JGR Earth Surface

RESEARCH ARTICLE
10.1029/2020JF005587

Atmospheric and Oceanographic Signatures in the Ice Shelf Channel Morphology of Roi Baudouin Ice Shelf, East Antarctica, Inferred From Radar Data

R. Drews[1], C. Schannwell[1], T. A. Ehlers[1], R. Gladstone[2], F. Pattyn[3], and K. Matsuoka[4]

[1]Department of Geoscience, University of Tübingen, Tübingen, Germany, [2]Arctic Centre, University of Lapland, Rovaniemi, Finland, [3]Laboratoire de Glaciologie, Université Libre de Bruxelles, Brussels, Belgium, [4]Norwegian Polar Institute, Tromsø, Norway

Key Points:
- The radar stratigraphy in ice shelves is 9 times more sensitive to variability in snow deposition than to variability in basal melting
- Some ice shelf channels at Roi Baudouin Ice Shelf deflect from flowlines; the radar stratigraphy reflects related processes
- Variable snow deposition causes slow deflection, and basal melting can form ice shelf channel junctions far from the grounding line

Supporting Information:
- Supporting Information S1

Correspondence to:
R. Drews,
reinhard.drews@uni-tuebingen.de

Citation:
Drews, R., Schannwell, C., Ehlers, T. A., Gladstone, R., Pattyn, F., & Matsuoka, K. (2020). Atmospheric and oceanographic signatures in the ice shelf channel morphology of Roi Baudouin Ice Shelf, East Antarctica, inferred from radar data. *Journal of Geophysical Research: Earth Surface*, *125*, e2020JF005587. https://doi.org/10.1029/2020JF005587

Received 3 MAR 2020
Accepted 20 APR 2020
Accepted article online 26 APR 2020

Abstract Ice shelves around Antarctica can provide back stress for outlet glaciers and control ice sheet mass loss. They often contain narrow bands of thin ice termed ice shelf channels. Ice shelf channel morphology can be interpreted through surface depressions and exhibits junctions and deflections from flowlines. Using ice flow modeling and radar, we investigate ice shelf channels in the Roi Baudouin Ice Shelf. These are aligned obliquely to the prevailing easterly winds. In the shallow radar stratigraphy, syncline and anticline stacks occur beneath the upwind and downwind side, respectively. The structures are horizontally and vertically coherent, except near an ice shelf channel junction where patterns change structurally with depth. Deeper layers truncate near basal incisions. Using ice flow modeling, we show that the stratigraphy is ~9 times more sensitive to atmospheric variability than to oceanic variability. This is due to the continual adjustment toward flotation. We propose that syncline-anticline pairs in the shallow stratigraphy are caused by preferential snow deposition on the windward side and wind erosion at the downwind side. This drives downwind deflection of ice shelf channels of several meters per year. The depth variable structures indicate formation of an ice shelf channel junction by basal melting. We conclude that many ice shelf channels are seeded at the grounding line. Their morphology farther seaward is shaped on different length scales by ice dynamics, the ocean, and the atmosphere. These processes act on finer (subkilometer) scales than are captured by most ice, atmosphere, and ocean models, yet the dynamics of ice shelf channels may have broader implications for ice shelf stability.

Plain Language Summary Ice flows from Antarctica's interior toward the coast. At the contact point between ice and ocean, the ice becomes afloat and forms fast-flowing ice shelves. Snowfall continuously accumulates at the ice shelf surface, and at the ice shelf bottom the relatively warm ocean water can melt ice from below. Ice shelves sometimes exhibit a network of surface depressions resembling a river network. At the base, the depressions are accompanied by large incisions termed ice shelf channels. Using radar as a tool for echolocation, we investigate how the shape of this network is formed. We find that snow preferentially collects in the upwind side of the surface depressions. This makes ice shelf channels move to the downwind side. We also find that ice shelf channels can form junctions through localized ocean melting. This is important because it helps us to better understand how the Antarctic ice sheet interacts with the surrounding ocean.

1. Introduction

Most of the Antarctic ice sheet is fringed by ice shelves, many of which damp upstream ice discharge through buttressing (Dupont & Alley, 2005; Fürst et al., 2016). Disintegration of ice shelves can cause ice sheet mass loss and sea level rise (e.g., Rack & Rott, 2004; Schannwell et al., 2018). Ice shelf channels are 0.5–5 km wide, curvilinear bands of thin ice dissecting many Antarctic and Greenlandic ice shelves in the along-flow direction (Alley et al., 2016). They may weaken ice shelves through fracturing (Dow et al., 2018; Rignot & Steffen, 2008; Vaughan et al., 2012) or strengthen them by either evacuating surface melt water (Bell et al., 2017) or reducing overall ocean-driven melting at the ice shelf base (Gladish et al., 2012; Millgate et al., 2013). These competing processes make it difficult to evaluate the net impact of ice shelf channels on ice shelf stability. Moreover, there are few observations on how the ice thickness gradient, with a depression at the surface and an incision at the ice shelf base, drives ice dynamic (e.g., channel closure), atmospheric

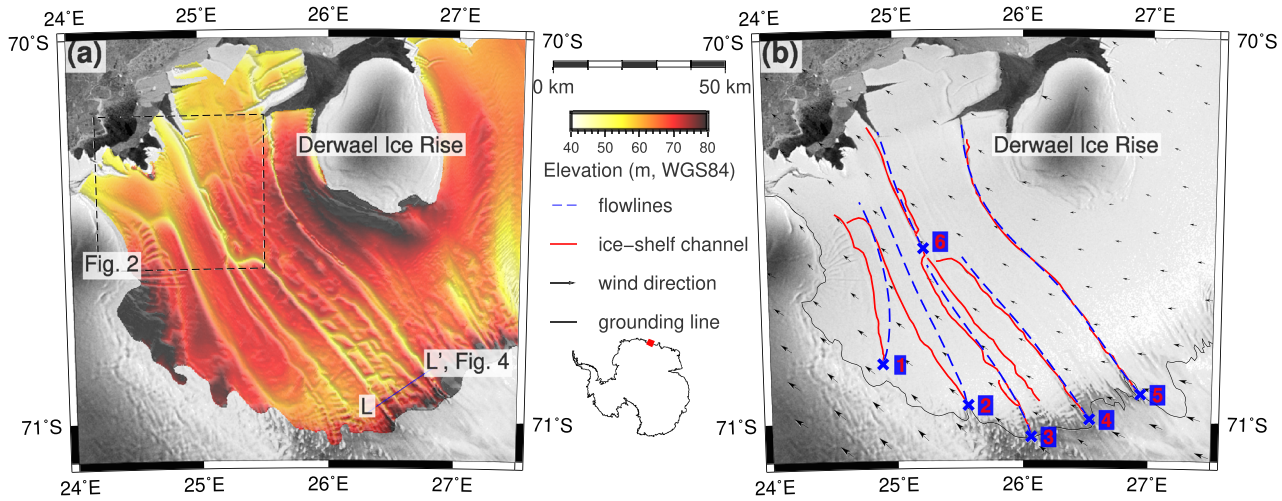

Figure 1. (a) Ice shelf channel network in the Roi Baudouin Ice Shelf apparent as depressions in the surface elevation (Berger et al., 2016) shown for the floating areas only. A number of ice shelf channel junctions are evident. Location of Figure 2 is marked with the dashed black lines. (b) Selected ice shelf channels. The numbers 1–6 mark individual ice shelf channel referred to in the main text. Blue crosses mark starting points of corresponding flowlines (calculated from surface velocities from Mouginot et al., 2012). Long-wavelength deflections are evident for channel-flowline pairs 1, 2, and to a lesser degree also for 3, 4, and 6. Background is the Radarsat Mosaic (Jezek, 2003) with arrows demonstrating the mean wind direction from Lenaerts et al. (2014).

(e.g., wind drift), and oceanic (e.g., localized basal melting) processes seaward of the grounding line. In this study, we identify signatures of these processes in the ice shelf stratigraphy and evaluate how they contribute to the overall ice shelf channel morphology. Our aim is to quantify the mechanisms operating within ice shelf channels and to identify the spatial and temporal scales of processes required to adequately capture ice shelf buttressing in coupled ice ocean models (Asay-Davis et al., 2016; Goldberg et al., 2019).

Previous work has made significant progress in understanding the nature of ice shelf channels. Basal melting can be localized within ice shelf channels (Berger et al., 2017; Dutrieux et al., 2013; Dutrieux et al., 2014; Gourmelen et al., 2017; Marsh et al., 2016; Rignot & Steffen, 2008; Stanton et al., 2013; Shean et al., 2018; Washam et al., 2019). The basal grooves under ice shelves modify subshelf ocean circulation in the entire ice shelf cavity (Gladish et al., 2012; Mankoff et al., 2012; Millgate et al., 2013). Proposed sources for ice shelf channels near the grounding line include subglacial water conduits (Jenkins, 2011; Le Brocq et al., 2013; Marsh et al., 2016), overriding of basal obstacles upstream of the grounding line (Drews et al., 2017; Gladish et al., 2012; Jeofry et al., 2018), transverse variability of ice shelf thickness at the grounding line (Sergienko, 2013), or self-organization between ocean-driven melting and ice thinning (Alley et al., 2016; Gourmelen et al., 2017). Once initiated, ice shelf channels will slowly close if no other processes are active (Drews, 2015; Wearing et al., 2018). However, their geometry and underlying ocean circulation can coevolve further in ways that are not fully understood as the small spatial and temporal scales involved are at the resolution limit of ice and ocean models (Sergienko, 2013).

All ice shelf channels advect with ice flow. Satellite imagery shows systematic deviations from flowlines calculated from surface velocities (Greene et al., 2017; Mouginot et al., 2012). We consider the possibility that ice flow direction has changed over time later and first focus on two aspects in the ice shelf channel morphology: (1) long-wavelength deflections, which we define as a monotonically increasing misfit between the observed ice shelf channel location and a corresponding flowline; and (2) ice shelf channel junctions where two or more ice shelf channels meet. For example, Channels 1 and 2, and to a lesser extent Channels 3, 4, and 6 demonstrate a leftward deflection (Figure 1, where left and right are defined relative to the ice flow direction). The close-up in Figure 2 shows bifurcating (e.g., J2) and converging (e.g., J1, J3, and J4) junctions, again relative to the ice flow direction.

We distinguish to what extent the ice shelf channel morphology seeded near the grounding line is modified farther seaward. Processes at the grounding line include, for example, a migration of subglacial water conduits. Farther seaward, biased basal melting due to Coriolis effects, or biased deposition of snow caused by wind drift, may cause ice shelf channels to deflect. Figure 3 summarizes two end-member hypotheses relevant for ice shelf channel morphology. These include the following: Ice shelf channel deflections are

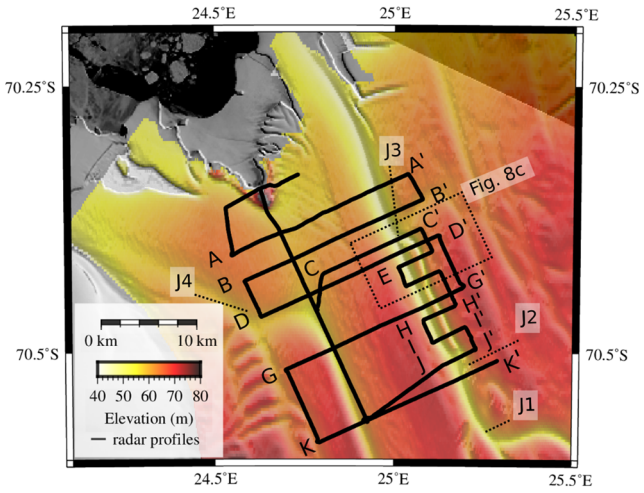

Figure 2. Close-up locating radar transects covering two major ice shelf channels (2, 6 labeled in Figure 1), and one minor ice shelf channel which first bifurcates (J2) and then merges back (J3) to Ice Shelf Channel 6. Profile C-C has been measured both in 2012 and 2014.

caused exclusively by oceanic or atmospheric processes acting on the ice shelf (Hypothesis 1) or deflections are caused only by a migration of the sources at the grounding line (Hypothesis 2). Correspondingly, ice shelf channel junctions may be formed by localized basal melting (Hypothesis 1) or by merging/splitting of the corresponding sources at the grounding line (Hypothesis 2). A principal difference is that processes in Hypothesis 1 can occur over long time scales (i.e., hundreds of years during advection to the calving), whereas processes linked to Hypothesis 2 are limited to shorter time intervals (i.e., tens of years during advection through the grounding zone).

To evaluate these hypotheses, we exploit the geometry of the isochronal radar stratigraphy as a window into the ice dynamic, atmospheric, and oceanographic history that the ice shelf channel has experienced. Radar isochrones represent former ice sheet surfaces, which are subsequently buried by snowfall and deformed by ice flow. Interpretation of the isochrone geometry is not unequivocal, and, as we will show later, atmospheric variability appears more prominent compared to the oceanic component. Nevertheless, we find patterns in the isochrone geometry documenting the deflection of ice shelf channels, and also evidence for formation of an ice shelf channel junction far away from the grounding line. Our new findings do not explain the full complexity in the ice shelf channel morphology, but they highlight that interpretation of the morphology

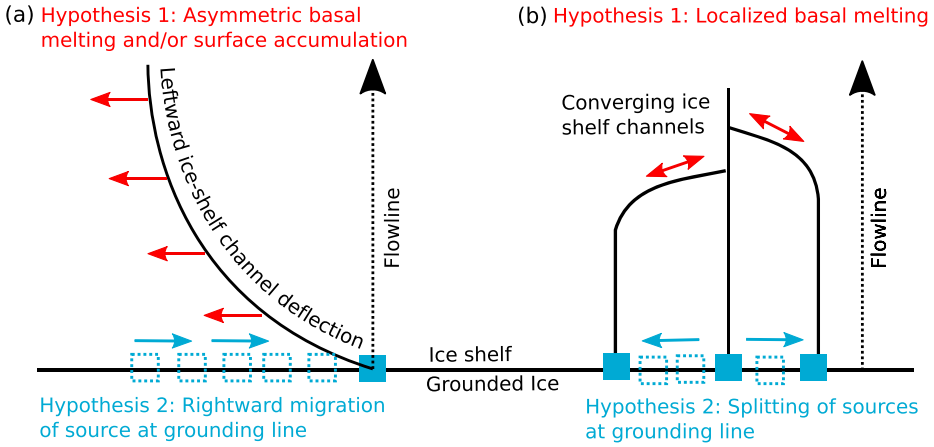

Figure 3. Bird's eye view of competing hypotheses explaining long-wavelength deflections of ice shelf channels from flowlines (a) and formation of ice shelf channel junctions (b). In both cases, the observed morphology can either be explained with processes occurring at the grounding line (e.g., migration and splitting of subglacial water conduits), or with processes acting during ice shelf channel advection (e.g., deflection through asymmetric basal melting or surface accumulation, junction formation through localized basal melting).

requires integration of a number of different mechanisms including patterns of surface accumulation and basal melting seaward of the grounding line. Disentangling the different contributions will unlock the ice shelf channel morphology as an important ice dynamic, oceanographic, and atmospheric proxy over the last few centuries and also improve our understanding of ice shelf stability.

2. The Roi Baudouin Ice Shelf

The Roi Baudouin Ice Shelf in East Antarctica is traversed by a number of ice shelf channels. Many, but not all, of these originate at the grounding line (Figure 1). Drews et al. (2017) suggested that ice shelf Channels 4 and 5 are formed by grounded ice overriding basal obstacles upstream of the grounding line. Farther downstream, ice shelf channels were investigated with ground-penetrating radar and stake arrays (Drews, 2015; Drews et al., 2017). The previous work found that the wider ice shelf channels are in hydrostatic equilibrium and that significant marine ice accretion is unlikely. The data also reveal a localized shear zone with a step change in along-flow velocities across an ice shelf channel. We integrate these findings into our analysis pertaining to the ice shelf stratigraphy. We selected this site for our study as the radar profiles cover two ice shelf channels deflecting leftward (westward) and also image Ice Shelf Channel Junctions J2 and J3 (Figure 2).

The ocean conditions around and under Roi Baudouin Ice Shelf result in moderate net basal melt/freezing rates with a spatial average of approximately -0.8 m a^{-1} (negative values defining mass loss). Spatial variability increases toward the grounding zone (Berger et al., 2016). There, basal melting peaks at several meters per year during the austral summer and drops to near 0 during the austral winter (Sun et al., 2019).

Atmospheric circulation is dominated by katabatic winds and synoptic precipitation events. The mean wind direction is from east and southeast when katabatic forcing is dominant (Figure 1b). However, the main moisture flux is directed into the southwesterly direction and therefore near perpendicular to the ice shelf channel orientation (Lenaerts et al., 2014). Those precipitation events are also manifested in a gradient of net surface accumulation/ablation rates across Derwael Ice Rise located within the Roi Baudouin Ice Shelf (Drews et al., 2016). Although Philippe et al. (2016) find a recent increase in the surface accumulation rates since the twentieth century, Callens et al. (2016) established that the spatial pattern has likely been stable for many hundreds of years. This temporal stability is the relevant time scale for ice shelf channel morphology as mean advection time from the grounding line to the ice shelf front is about 400 years. Near the grounding line, wind-albedo interactions result in significant surface melt infiltrating into the firn column dilluting the shallow radar stratigraphy (Lenaerts et al., 2017). Farther seaward, continuous surface accumulation results in a well-defined radar stratigraphy, which we observe in our shallow radar transects near the ice shelf front. We use net surface accumulation/ablation rates from an atmospheric climate model run on a 5.5 km grid (Lenaerts et al., 2014). Smaller-scale effects such as wind sheltering and wind erosion across surface undulations are consequently not captured. Those may be important mechanisms contributing to the observed ice shelf channel deflections. The atmospheric circulation patterns and the comparatively low net basal melt/freezing rates encountered at Roi Baudouin Ice Shelf are representative for most ice shelves in Dronning Maud Land. The inferences drawn here may also be relevant for other ice shelves which are situated in cold water basins and experience significant surface accumulation.

3. Methods

3.1. Internal Ice Stratigraphy and Thickness From Ground-Penetrating Radar

Ground-penetrating radar can measure the internal stratigraphy and thickness of ice. The internal stratigraphy is caused by changes in density, conductivity, and ice fabric (Fujita et al., 2006). The majority of the internal reflection horizons are isochrones (Eisen et al., 2004). After deposition of the reflection horizons at the surface, they migrate with time to greater depths where they are increasingly deformed by ice flow. We have imaged the shallow stratigraphy (<50 m depth) with a 400 MHz radar and the deeper stratigraphy with a 10 MHz radar. Surface elevation and the position of the radar were measured using Global Navigation Satellite System receivers. Using time stamps, we gridded the GPS and the two radar data sets to common postings with 25 m spacing. The vertical resolution of the radar data is <20 m for the 10 MHz antenna and <0.5 m for the 400 MHz antenna. Both the 400 and the 10 MHz data image the internal ice stratigraphy in many areas throughout their respective depth windows. The ice shelf channel flanks, where the internal stratigraphy is often steeply inclined and internal layers are more closely spaced, are challenging to interpret. Moreover, we encounter some areas of a weak dielectric contrast, particularly near the grounding zone where surface melt water infiltration is significant.

The majority of the data were collected in 2012 and have previously been discussed by Drews et al. (2015) where details of data acquisition and processing are also described. An additional survey in 2014 revisited Profile C-C with the 400 MHz system (Lenaerts et al., 2017). In a Lagrangian reference frame moving with ice shelf flow, the 2012 profile is located about 500 m downstream of the 2014 transect. We neglect the 2-year time difference between those profiles and treat them as two transects collected at different locations in the fixed Eulerian reference frame of 2012. The internal stratigraphy of all radar transects is analyzed to better understand the formation of the ice shelf channel morphology which has not previously been investigated. We also combine it with unpublished data of the 10 MHz radar collected in 2016 near the grounding line (Figure 4).

3.2. Age-Depth Profile and Vertical Velocities in Firn

To estimate the age of the shallow stratigraphy, we use an approximation of the age equation linked to an ice core based density profile retrieved within our study area (Hubbard et al., 2013). The approximation is one-dimensional and neglects horizontal advection. We justify this by using the corresponding depth-age estimate only for the shallow radar layers, which have not yet experienced significant strain thinning. The age-depth relationship is governed by

$$u_z(z)\frac{\partial A}{\partial z} = 1 \tag{1}$$

$$\rho\frac{\partial u_z}{\partial z} + u_z\frac{\partial \rho}{\partial z} = 0 \tag{2}$$

with A referring to the age at depth z, given a vertical velocity (positive downward) u_z including densification with the density profile $\rho(z)$. Equation (1) is the steady-state form of the age equation, and equation (2) is conservation of mass in compressible firn (Eisen, 2008). The density inferred by Hubbard et al. (2013) increases exponentially with depth:

$$\rho(z) = \rho_i - (\rho_i - \rho_s)e^{-kz} \tag{3}$$

using ice density $\rho_i = 910$ kg m^{-3}, surface snow density $\rho_s = 450$ kg m^{-3}, and a densification factor $k = 0.033$ m^{-1}. Equations (1) and (2) are separable (Appendix (A)) resulting in the depth-age estimate of

$$A(z) = \frac{\rho_i - \rho_s}{c_1 k}e^{-kz} + \frac{\rho_i}{c_1}z + c_2 \tag{4}$$

and a near-surface vertical velocity of:

$$u_z = c_1\frac{e^{kz}}{\rho_i(e^{kz} - 1) + \rho_s} \tag{5}$$

The integration constants c_1 and c_2 contain the surface density and the net surface accumulation/ablation rates (Lenaerts et al., 2014). To account for uncertainties, we additionally consider the lowest and highest rates encountered at the Roi Baudouin Ice Shelf.

3.3. Vertical Velocities for Deeper Ice in Ice Shelves

The depth variation of isochronal radar layers in across-flow transects reflects much of the variability in the corresponding vertical submergence velocities. It is therefore useful to derive an analytical expression for the vertical velocities in ice shelves highlighting the principle mechanisms at work. They are approximated analytically in Appendix B with

$$u_z(z) = \underbrace{\dot{a}\frac{\rho_i}{\rho_w} - \dot{b}\left(1 - \frac{\rho_i}{\rho_w}\right)}_{\text{column adjustment}} + \underbrace{\left(H(1 - \frac{\rho_i}{\rho_w}) + z\right)\frac{\partial u_x}{\partial x}}_{\text{along-flow stretching/compression}} \tag{6}$$

Here, $\dot{a}$ is the net surface accumulation/ablation rate (in m a^{-1} ice equivalent, positive for mass gain); $\dot{b}$ is net basal melting/refreezing rate (in m a^{-1} ice equivalent, negative for mass loss); H is the ice thickness; ρ_i and ρ_w are the densities of ice and ocean water, respectively; we set depth $z = 0$ at the ice surface and

choose u_x for the velocity in the along-flow direction x. Equation (6) shows the well-known linear depth dependence of the vertical velocity, which results from the simplifying assumptions of the shallow-shelf approximation (Morland, 1987). The first two terms on the right-hand side of equation (6) represent the ice column adjustment as a result of $\dot{a}$ and $\dot{b}$. The third term accounts for dynamic thinning/thickening in the along-flow direction.

3.4. Ice Velocities and Age for Deeper Ice in Ice Shelves From Numerical Modeling

The thickness gradient across ice shelf channels results in a flow regime that requires consideration of all stress gradients in the underlying force balance (Drews et al., 2015). Some of the ice flux is directed from outside the channel toward the channel's center, making the vertical velocity profile with depth nonlinear. This is not included in the shallow shelf approximation applied previously. The ice flow model Elmer/Ice (Gagliardini et al., 2013) is used to predict the geometry of isochronal layering for different atmospheric and oceanographic forcings. Elmer/Ice solves the full Stokes stress balance equations, and here this is done for a synthetic 2-D cross section of a freely floating ice shelf (Figure 5). The cross section contains a prescribed ice shelf channel with comparable dimensions to those observed in our radar data. The shape along distance x is described with a Gaussian function at the surface S and the base B using hydrostatic equilibrium:

$$S(x) = (1 - \frac{\rho_i}{\rho_w}) \left(\bar{H} - C_0 e^{-\frac{x^2}{2\sigma^2}} \right) \tag{7}$$

$$B(x) = -\frac{\rho_i}{\rho_w} \left(\bar{H} - C_0 e^{-\frac{x^2}{2\sigma^2}} \right) \tag{8}$$

where ρ_i and ρ_w are densities of ice and ocean water, $\bar{H}$ is the mean ice thickness away from the ice shelf channel, C_0 determines the initial amplitude of the ice shelf channel, and σ its initial width. The model inputs are different combinations of $\dot{a}$ and $\dot{b}$. $\dot{a}$ has constant value ($\dot{a}_0$) away from the ice shelf channel and varies with changing surface slope across ice shelf channels to investigate effects of wind sheltering on the upwind side and crest erosion on the downwind side. The magnitude of this variation is tuned with a factor (D_1) to approximate the observations from the shallow radar stratigraphy detailed below. $\dot{b}$ has the same spatial pattern simulating preferential melting due to Coriolis effects on one of the channel's flanks:

$$\dot{a}(x) = \dot{a}_0 + D_1 \frac{\partial S}{\partial x} \tag{9}$$

$$\dot{b}(x) = \dot{b}_0 + D_2 \frac{\partial B}{\partial x} \tag{10}$$

The factor D_2 is chosen so that the $\dot{a}$ has the same magnitude as $\dot{b}$. While those values are in the range of previous observations (Berger et al., 2017), there is no physical justification for choosing them to be equal. It results, however, in constant vertical velocities away from ice shelf channels so that the cross section does not thin or thicken over the simulation. This emphasizes the velocity anomalies across the ice shelf channels and makes the lateral migration of the channel easy to track. Changing the magnitude of the background rates does not significantly alter the migration behavior nor the signatures in the corresponding age-depth fields. The ice viscosity is isothermal and strain-rate dependent in accordance with Glen's flow law. We use a Glen exponent of $n = 3$ and a corresponding rate factor B, which has been used previously for modeling ice shelf flow in synthetic setups (e. g., Pattyn et al., 2012). There is evidence that $n = 3$ for ice shelves (Jezek et al., 1985), but it could also be higher (Goldsby & Kohlstedt, 2001). We explore the possibility for $n = 4$ with a corresponding rate factor determined by Bons et al. (2018) for Greenland, acknowledging that rate factors for Antarctic ice shelves could be very different. The node spacing in the finite element grid is <20 min the vertical and <60 min the horizontal. Both the surface and the base are treated as free boundaries evolving with kinematic boundary conditions. Transient adjustment of the ice thickness is stabilized with a viscous spring at the ice shelf base (Durand et al., 2009). Ice pressure is prescribed at the left and right boundaries, respectively (Figure 5). To calculate the isochrones, the age equation is solved using a semi-Lagrangian scheme by Martin et al. (2011). Age is initialized as a linear function of depth. This is based on the analytical solution to equation (1) for constant vertical velocities in ice.

Model parameters are detailed in Table 1. Primary model outputs in the 2-D geometry are the calculated vertical and across-flow velocities, together with the corresponding age-depth field. In all simulations the

Table 1
Model Parameters for Simulations of an Ice Shelf Transect

Parameter	Value	Units
ice density (ρ_i)	910	kg m^{-3}
ocean water density (ρ_w)	1,025	kg m^{-3}
ice thickness (H)	300	m
ice shelf channel RMS width (σ)	700	m
background net surface accumulation/ablation rate ($\dot{a}_0$)	0.3	m a^{-1}
background net basal melting/refreezing rate ($\dot{b}_0$)	0.3	m a^{-1}
tuning net surface accumulation/ablation rate (D_1)	0; 20	m a^{-1}
tuning net basal melting/refreezing rate (D_2)	0; −2.631	m a^{-1}
Glen exponent n	3;4	none
rate factor ($B, n = 3$)	$4.8{\cdot}10^{-24}$	s^{-1} Pa^{-3}
rate factor ($B, n = 4$)	$3.3{\cdot}10^{-29}$	s^{-1} Pa^{-4}

ice shelf channel migrates and progressively closes due to lateral inflow of ice into the channel. Therefore, all results are nonsteady state but represent a snapshot of the ice shelf channel geometry after 600 years.

4. Results

Section 4.1 reports distinct patterns in the radar stratigraphy across ice shelf channels. It also explains the larger sensitivity of the radar stratigraphy to variability in $\dot{a}$ compared to variability in $\dot{b}$. Modeling results (section 4.2) show how ice shelf channels can be deflected by spatially variable $\dot{a}$ or $\dot{b}$. The predicted radar signatures enable quantification of deflection rates from observations (section 4.3). We close with dating and backtracing transient patterns in the stratigraphy at Ice Shelf Channel Junction J3 (section 4.4). In the discussion, we interpret that persistent variability in $\dot{a}$ contributes to ice shelf channel deflection. The transient patterns in the stratigraphy are consistent with formation of the junction by localized basal melting.

4.1. Radar Signatures Observed in Transects Across Ice Shelf Channels

Ice shelf channels appear well developed a few kilometers downstream of the grounding line with basal incisions larger than 100 m (Figure 4). Plunging internal reflection horizons are evident for Ice Shelf Channels 4 and 5. At greater depth these are also truncated. Both channels have a long downstream continuation in the surface elevation model (Figure 1). The ice-ocean interface between those channels is rough, reflecting a number of converging junctions in the surface elevation model. There is no discernible shallow (<50 m depth) stratigraphy in this area due to surface melt water infiltration (Lenaerts et al., 2017).

The radar grid near the ice shelf front covers two major ice shelf channels (2 and 6) with 11 across-flow transects (Figure 2). Channel 6 exhibits two junctions (J2 and J3) with a smaller neighboring channel that

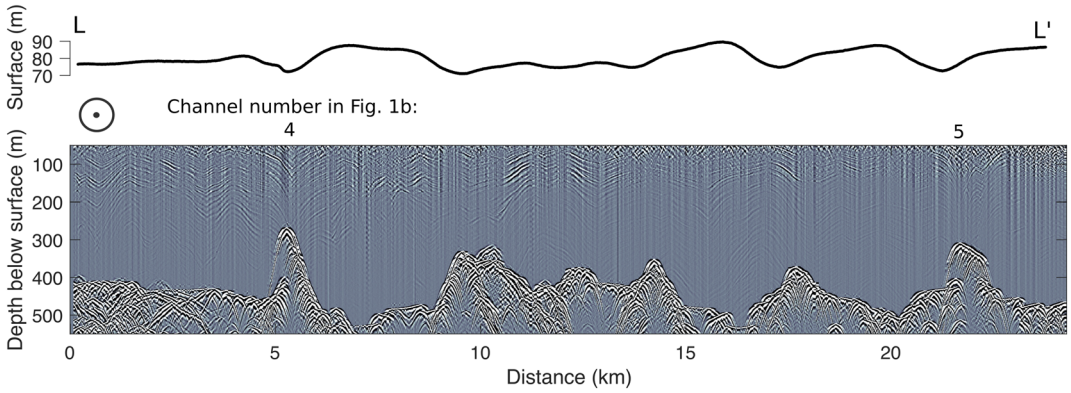

Figure 4. Radar transect a few kilometers downstream of the grounding line (located in Figure 1a) showing surface depressions (top) and basal incisions at the Ice-Shelf Channels 4 and 5. Truncated internal radar reflection horizons are visible in both ice-shelf channels.

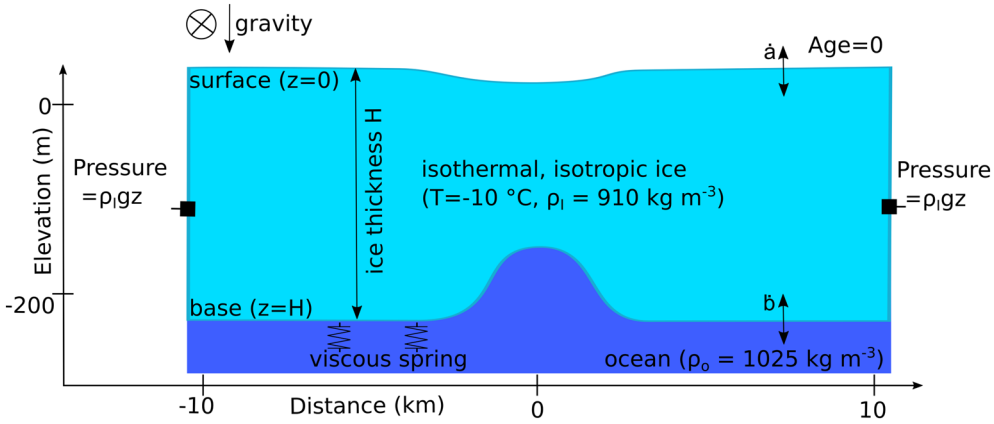

Figure 5. Sketch of the 2-D model domain with applied boundary conditions. Main ice-shelf flow direction is into the page. The applied net basal melting/freezing rates ($\dot{b}$) vary across the ice-shelf channel to simulate asymmetries due to Coriolis effects. Net surface accumulation/ablation rates ($\dot{a}$) vary to simulate wind sheltering on the upwind and crest erosion on the downwind side, respectively.

is approximately 13 km long. Figure 6 displays two typical cross sections showing all major signatures also visible in the other cross sections (supporting information): The ice-ocean interface within the large basal incisions appears smooth. Away from the basal incisions (e.g., at distances 7–10.5 km in G-G′), small basal grooves are evident. These are partially accompanied with near-surface reflection hyperbolas in the radar transects and with increased roughness in the GPS-based surface topography. The horizontal scales involved are <100 m and can thus barely be resolved with the 25 m grid posting of our data set. At distances 10.5–16 km we find a radar transparent zone starting at about 100 m depth. In other areas, the internal stratigraphy is intact throughout the entire ice column and a number of truncating internal reflection horizons are observed at the boundaries of the basal incisions.

At shallow to intermediate depths, characteristic syncline (i.e., downward warping) and anticline (i.e., upward warping) stacks of radar isochrones occur beneath the surface troughs of ice shelf channels. These stacks vary in amplitude but occur in all 11 transects. They distinctly stand out from the much

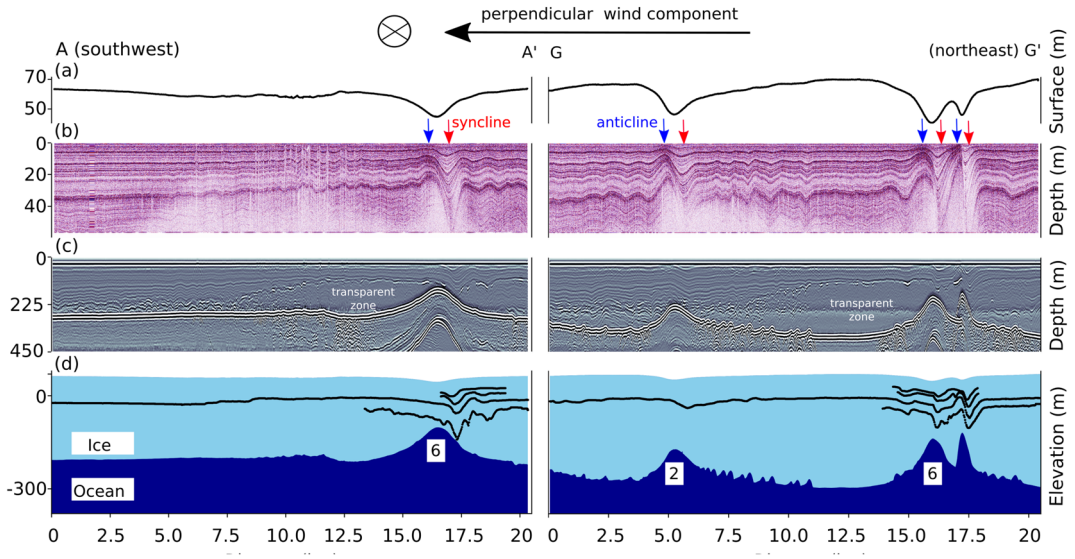

Figure 6. Radar Transects A-A′ and G-G′ imaging Ice Shelf Channels 2 and 6 (located in Figure 2) with surface topography (a), shallow internal radar stratigraphy (b), entire ice column (c), and the topographically corrected ice thickness relative to the WGS84 ellipsoid (d). Syncline and anticline stacks referenced in the text are marked with red and blue arrows, respectively. Black lines in (d) are picked radar horizons.

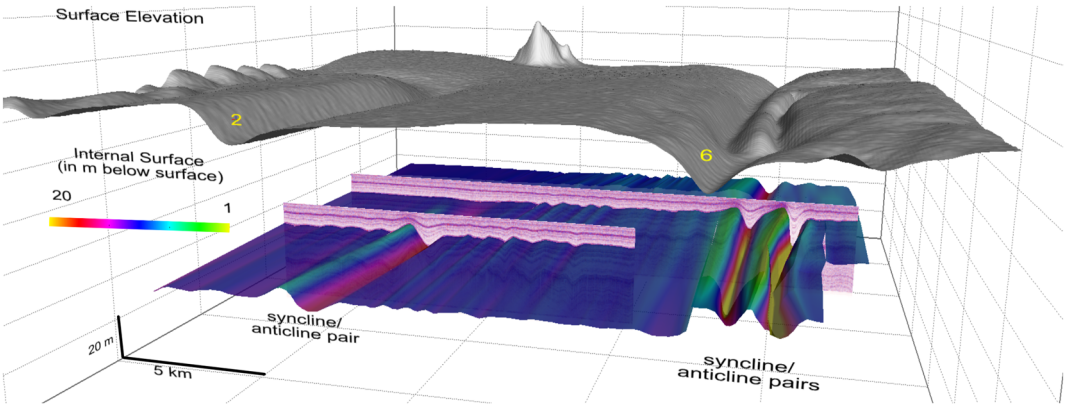

Figure 7. Perspective view into the along-flow direction. Surface depressions of Ice Shelf Channels 2 and 6 are shown in gray. An internal reflection surface interpolated from all radar cross sections is shown in color as depth below surface. The two surfaces are vertically offset to improve visibility. Syncline/anticline pairs associated with the surface depressions are the dominant patterns in the shallow stratigraphy of all cross sections.

more homogenous stratigraphy in areas where the ice thickness varies less strongly. Horizontally, the syncline/anticline stacks can be connected in the along-flow direction (Figure 7). Vertically, the stacks are tilted and offset toward the northeast relative to the lowest point at the surface (Figure 6). The tilt is strongest near the surface. Syncline stacks in the deeper radar stratigraphy are aligned near vertically. The maxima of the anticline stacks are difficult to track, partially merging and even cropping out near the surface (e.g., at distance 17 km in G-G′). The synclines, on the other hand, are easier to track and their amplitude (i.e., difference between depth outside and inside the syncline) increases near linearly with depth. Their ratio (i.e., fraction between depth outside and inside the syncline) averages at ∼1.5 (Figure 8). In all but two of the transects, the syncline/anticline amplitudes increase with depth but do otherwise not show a structural change. An exception is illustrated for the two radar transects C-C′ crossing Ice Shelf Channel Junction J3 (Figure 9). In these profiles, synclines change in width and partially decrease in amplitude with depth. We will consider this later (section 4.4).

Formation of synclines and anticlines in the radar stratigraphy relate to variability in the vertical velocities. Analysis in section 3.3 shows that this variability is much more sensitive to $\dot{a}$ than to $\dot{b}$. This is because in the column adjustment term of equation (6), $\dot{a}$ is multiplied with a factor of 0.9 (with $\rho_i \sim 900$ kg m^{-3} and $\rho_w \sim 1,000$ kg m^{-3}), whereas $\dot{b}$ is multiplied with a factor of 0.1. More adjustment to flotation is required for mass added (removed) at the surface compared to the same mass gained (lost) at the ice shelf base. It follows that the radar stratigraphy in ice shelves is about nine times more sensitive to variability in $\dot{a}$ than to variability in $\dot{b}$. We treat this more rigorously and independent of the shallow shelf approximation, using numerical modeling next. We focus on the shallow syncline/anticline stacks, considering them as proxies for the recent evolution of ice shelf channels.

4.2. Ice Shelf Channel Deflection Through Variability in Surface Accumulation and Basal Melting

Elmer/Ice simulations with a spatially uniform $\dot{a}$ and $\dot{b}$ (not shown) result in a stationary ice shelf channel gradually decreasing in size due to lateral inflow of ice into the channel (here by about 15% over 600 years). This inflow is dependent on a number of factors such as the Glen exponent n, rate factor B, and the pressure boundary conditions. The signature of ice shelf channel closure on the predicted isochrones is small.

Ice shelf channels deflect in simulations where $\dot{a}$ or $\dot{b}$ change with ice thickness (Figure 10). The deflection direction is toward the minimum rates in both cases, that is, toward the location of maximum ice thinning. For the case of variable $\dot{a}$, this is because preferred snow deposition on the upwind side causes local thickening, and snow erosion on the downwind causes local thinning. The same argument holds for a corresponding variability in $\dot{b}$. The deflection rates are several meters per year, independent of whether deflection is caused by variability of $\dot{a}$ or $\dot{b}$ (Figures 10a and 10b). The effects are additive: Deflection rates double when both $\dot{a}$ and $\dot{b}$ are functions of ice thickness (Figure 10c).

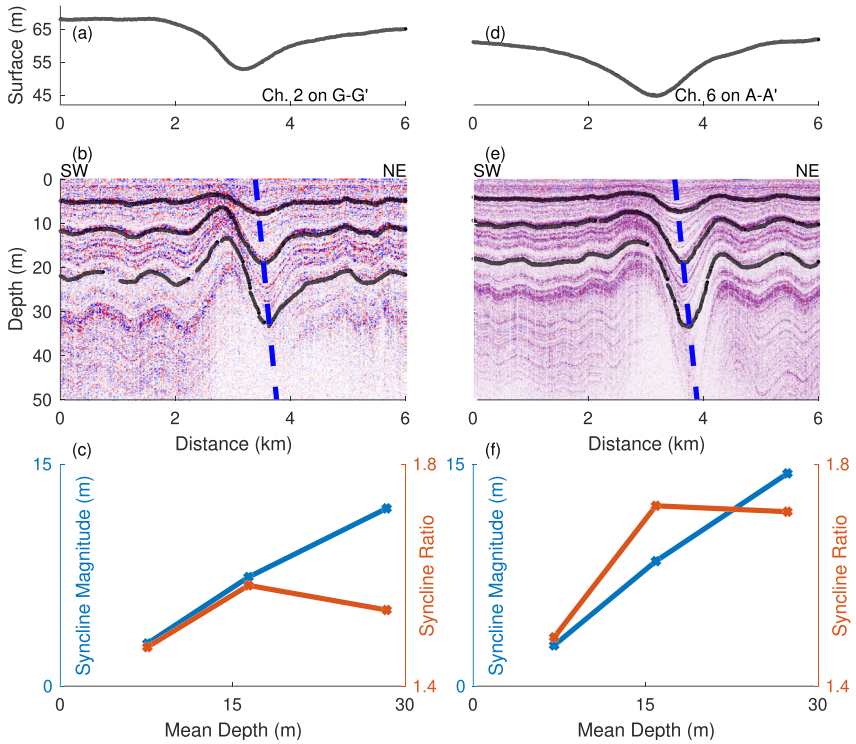

Figure 8. Characteristics of the shallow syncline stacks in the radar stratigraphy across Ice Shelf Channels 2 (a–c) and 6 (d–f). The troughs of the corresponding surface depressions (a, d) are slightly offset toward the southwest relative to the tilted synclines stacks observed in the 400 MHz radar data (b, e). The syncline amplitude (difference in depth between radar horizon outside and inside the syncline) increases near linearly with depth, resulting in an average syncline ratio (ratio of layer depth inside and outside the syncline) of 1.5 for Channel 2 and 1.6 for Channel 6.

The predicted internal radar stratigraphy is a proxy for the variability of $\dot{a}$ and $\dot{b}$ in two ways. First, although $\dot{a}$ and $\dot{b}$ have equal spatial variability, the former results in much larger syncline/anticline amplitudes. This is consistent with results from the previous section. Second, in both cases the syncline/anticline amplitudes increase with depth and are tilted. Near the surface, the tilt is proportional to the migration velocity. At larger depths, the tilt decreases because lateral inflow increasingly moves the syncline structure more toward the ice shelf channel center. The simulations thus reproduce some of the dominant patterns in the observed radar stratigraphy. The differing sensitivities of the ice shelf stratigraphy toward atmospheric and oceanic perturbations are now quantified analytically and numerically. This will lead later to the interpretation that

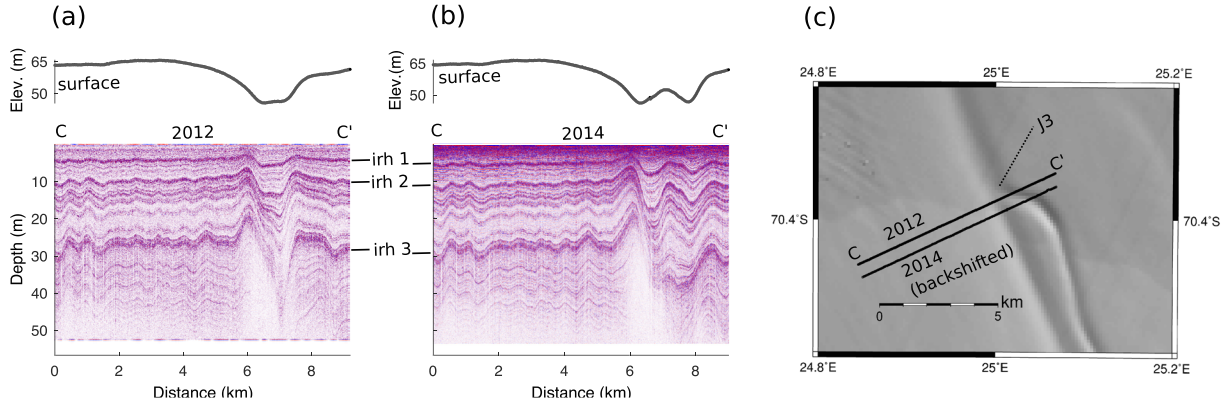

Figure 9. Structural changes of the synclines with depth at an ice shelf channel junction. Unlike in the shallow stratigraphy elsewhere (e.g., Figure 8) the syncline amplitudes do not gradually increase with depth but narrow (a) and merge with increasing depth (b). Profile in (a) was acquired in 2012, and profile (b) along the same coordinates in 2014. The profile locations are shown for the 2012 reference frame in (c).

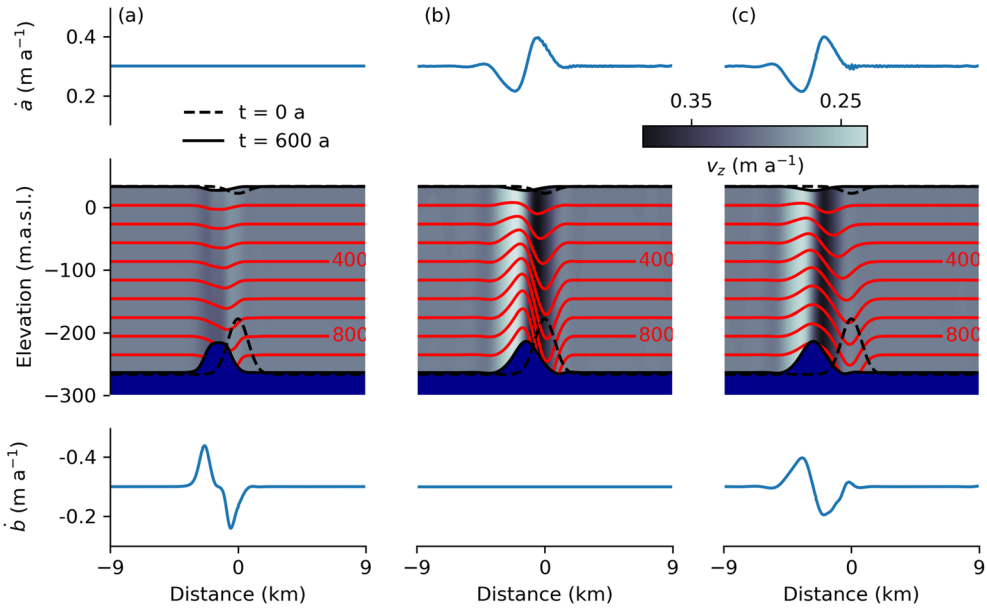

Figure 10. Modeled ice shelf channel geometry after 600 years of forcing with spatially variable net basal melting/freesing rates ($\dot{b}$, negative for mass loss) (a), spatially varying net accumulation/ablation rates ($\dot{a}$, positive for mass gain) (b) and both (c). Both $\dot{b}$ and $\dot{a}$ are functions of the surface and basal gradients, respectively. The red contours are isochrones in years, and the background colors mark the vertical velocities (positive downward) illustrating that variability in $\dot{a}$ induces a much stronger perturbation in the isochronal structure than corresponding variability in $\dot{b}$.

the strongest contributor to the observed syncline/anticline patterns is persistent variability in $\dot{a}$ (section 5.1). However, independent of the specific mechanism, the simulations show that the tilt in the shallow syncline/anticline stacks relates to ice shelf channel deflection rates.

4.3. Ice Shelf Channel Deflection Rates From the Shallow Radar Stratigraphy

The shallow syncline/anticline stacks (Figure 8) can be dated using the approximated vertical velocities and corresponding age-depth profile (Figure 11). We pick the syncline minima as a function of depth and estimate deflection rates from the slope of the age-distance regression. This results in deflection rates ranging from 3–5 m a^{-1}. Given that a typical advection time of ice shelf channels in the Roi Baudouin Ice Shelf is

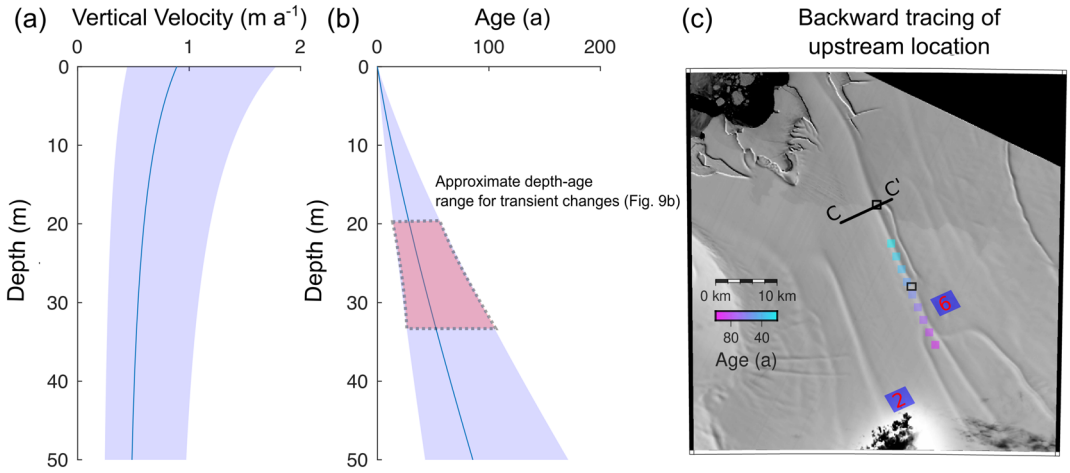

Figure 11. Modeled vertical velocities in the firn column for a range of net surface accumulation/ablation rates (a) and resulting depth-age profile (b). The depth range of the variable shallow radar stratigraphy marking transient changes (Figure 9) is highlighted with a red polygon. We use this time interval for backtracing in (c) estimating the location on the ice shelf where the transient changes likely occurred. Location of bifurcating and converging junctions are marked with black rectangles.

around 400 years (Drews et al., 2017), these deflection rates may result in a long-wavelength deflection of more than 1.5 km relative to a flowline originating at the grounding line. The deflection direction is given by the direction of the tilt. In our case, the tilt is toward the West, consistent with the observed deflections of ice shelf channels from their corresponding flowlines (Figure 1b).

4.4. Recent Modification of An Ice Shelf Channel Junction

The two profiles collected at C-C in 2012 and 2014 image the vicinity of Ice Shelf Channel Junction J3 . We position the 2014 into the 2012 reference frame by correcting for ice shelf motion (Figure 9c). The 2-year time difference is otherwise neglected. Contrary to all other transects, we observe a depth-variable structure in the 2014 radar stratigraphy indicating a transient change. In the 2012 profile, the lateral extent of the synclines decreases with depth while the syncline amplitudes, in common with most transects (see supporting information), increase with depth. For the 2014 profile, two shallow syncline stacks, tilted in opposite directions, transition to one joint syncline stack at greater depths. Syncline amplitudes decrease with depth unlike in all other transects. The structural change occurs in a depth range of 20–35 m corresponding to an age range of 16–124 years. Backtracing of the oldest age estimate along a flowline limits the upstream origin of this change to the center of today's ice shelf (Figure 9c). We will interpret this later as possible evidence for localized basal melting forming an ice shelf channel junction (section 5.3).

5. Discussion

5.1. Distinguishing Between Atmospheric and Oceanic Signatures in the Ice Shelf Stratigraphy

For synclines/anticlines in the ice shelf stratigraphy, there is no clear way to differentiate between atmospheric and oceanic contributions because the column adjustment is given by the sum of both (equation (6)). Synclines can be caused by local variations in $\dot{a}$ or $\dot{b}$ or both. The key to distinguishing between the different contributions is the differing sensitivity in terms of shaping the ice shelf stratigraphy. Any given syncline requires variability in $\dot{b}$ that is 9 times larger compared to the variability required by $\dot{a}$ for forming the same syncline (section 3.3). Vice versa, the same spatial variability in $\dot{a}$ and $\dot{b}$ results in much smaller syncline amplitudes for the latter (Figures 10a and 10b).

In the radar transects, the depth ratio between an internal reflection horizon outside and inside the synclines averages around 1.5 (Figures 8c and 8f). Considering column adjustment only, this requires locally increased $\dot{a}$ by a factor of ~1.7. Approximately 90% of this local mass gain will result in vertical submergence due to hydrostatic adjustment. Alternatively, the syncline can also reflect locally decreased $\dot{b}$ by a factor of ~15. In this case, only about 10% of the local mass loss will result in increased vertical submergence due to hydrostatic adjustment. Any combination between these two end-member cases is also possible. An obvious difference between the two scenarios is that the corresponding ice shelf channel becomes less incised in the along-flow direction in the case of elevated $\dot{a}$ and more incised for more negative $\dot{b}$. Such a change in ice thickness can be interpreted using mass conservation with high-resolution satellite data. Berger et al. (2017) did this analysis and found no significant signal for basal melting in ice shelf channels within our research area. Although uncertainties are large, a signal 15 times stronger than the background melt rate should have been apparent. We, therefore, conclude that the observed synclines are at least partially caused by a locally elevated $\dot{a}$ on the upwind side. The smaller anticlines correspond to a minimum in $\dot{a}$ on the downwind side. Quantification of wind erosion is more difficult here, because the maxima of anticlines tend to merge near the surface and cannot easily be distinguished. In fact, some of them outcrop at the surface (e.g., at 17 km in G-G′, Figure 6). Surface outcropping by wind erosion is similar to development of truncated layers at the base by ocean-driven melting.

The information on wind direction (Figure 1b), particularly the synoptic precipitation events moving in a southwesterly direction (section 2), are broadly consistent with our inferences. They are, however, not detailed enough to capture turbulence on subkilometer scales relevant for the surface depressions of ice shelf channels. Nevertheless, a number of previous studies have noted that $\dot{a}$ sensitively depends on the surface topography influencing wind erosion, drift, and deposition of snow at various spatial scales (Black & Budd, 1964; Drews et al., 2013, 2015; Eisen et al., 2004; Eisen, 2008; Lenaerts et al., 2019; Spikes et al., 2004). Particularly for ice shelf channels, Langley et al. (2014) report a similar increase of local snow deposition in the channel's surface depression on the Fimbul Ice Shelf. This ice shelf is located at the Dronning Maud Land Coast and is subject to similar atmospheric conditions to those at the Roi Baudouin Ice Shelf. In our case, the synclines are offset relative to the ice shelf channel troughs and anticlines occur at the opposite sides.

This variability in $\dot{a}$ can drive ice shelf channel deflection. Implications are twofold. First, satellite-based methods using more coarsely gridded $\dot{a}$ fields may incorrectly close the mass budget near ice shelf channels. This will result in a flawed estimate of $\dot{b}$. Second, if the resulting ice shelf channel deflection is quantified in the ice shelf channel morphology, too much weight may be given to other possible mechanisms such as migrating sources at the grounding line or asymmetric ocean-driven melting.

The dominance of variability in $\dot{a}$ in the ice shelf stratigraphy makes oceanic contributions difficult to find, but it does not mean that basal melting is absent. The truncating radar isochrones at the ice shelf base both near the grounding line (Figure 4) and also much farther downstream (Figure 6) are the clearest indicators for localized basal melting in our data. The basal grooves may be signs of basal terraces previously linked to vigorous basal melting (Dutrieux et al., 2014), but our spatial resolution is not good enough for a quantitative analysis. Also, we have no good explanation for the radar transparent zone occurring in all of our radar transects near the ice shelf front. The upper onset of this zone is too shallow to explain the absence of layering with a loss of system sensitivity, but whether low dielectric contrast or poor stratigraphic integrity are important will need to be investigated elsewhere.

5.2. Deflections of Ice Shelf Channels by Atmospheric and Oceanic Processes Seaward of the Grounding Line

The 2-D model domain aligned in the across-flow direction demonstrates basic principles of ice shelf channel deflection and closure. It does not account for variability in the along-flow direction. This variability may include changes in $\dot{a}$, $\dot{b}$, or lateral boundary conditions (e.g., compression or extension). Such changes will impact the geometry of isochrones, limiting our ability to compare our model and data. This could be mitigated in future studies by integrating strain rates derived from observed surface velocities. Nevertheless, the simulations clearly show that the previously identified variability in $\dot{a}$ across ice shelf channels will result in a downwind deflection. The isochrone geometry is a proxy for this deflection in-line with our observations. Our inferred deflection rates of several meters per year therefore explain at least some of the long-wavelength deflection patterns at the Roi Baudouin Ice Shelf (Figure 1). It does not explain why some ice shelf channels deflect more than others, and it is difficult to rank how important the asymmetry in $\dot{a}$ is relative to other mechanisms. We cannot fully resolve this conflict here. One possible explanation is variability in the surface depressions both in width and amplitude interacting differently with the wind and precipitation patterns. The same holds for the basal interface, where previously inferred left-biased ocean-driven melting due to the Coriolis force (Gourmelen et al., 2017; Sergienko, 2013) may also be more important for some channels and less for others. In our case, both mechanisms will deflect ice shelf channels into the same direction. Local variations in $\dot{b}$, however, will be masked in the internal stratigraphy as long as variability in $\dot{a}$ persists. In the future, both effects may be disentangled by inverting the observed radar stratigraphy in the along-flow direction.

5.3. Modification of Ice Shelf Channel Junctions in the Ice Shelf

The two radar transects along C-C′ image transient changes at the ice shelf channel junction. The time dependence is evidenced by the narrowing of synclines (Figure 9a) and by the merging of two synclines which additionally decrease in amplitude with depth (Figure 9b) and hence age. The time interval between 2012 and 2014 is irrelevant in this regard. Dating of the isochrones shows that the change has occurred in the center of Roi Baudouin ice shelf far away from the grounding line. As established above, a major factor for the observed syncline structure is spatial variability in $\dot{a}$. This variability is steered by existing surface depressions. The narrowing of synclines in the 2012 profile means in this context that the surface depression is wider today than it has been in the past. Two synclines at shallow depths and one syncline at larger depths in the 2014 profile, correspondingly requires a transition from two surface depressions today to one surface depression in the past. This means that the 2014 transect first contained one ice shelf channel in the past and now contains two. Based on our age-depth model, the transition likely started approximately 120 years ago.

A possible scenario explaining this is as follows: At Time Step 1 (Figure 12a), the transect at first only contained one, comparatively narrow ice shelf channel deflecting leftward as evidenced by the tilted syncline stack. The other radar profiles indicate existence of two ice shelf channels farther upstream at this time, given the persistent synclines patterns seen in Profiles D–K. At Time Step 2 (Figure 12b), the transect witnessed development of a second channel resulting in the formation of two syncline stacks formed by $\dot{a}$. At Time Step 3 (Figure 12c), both ice shelf channels deflect in opposing directions leading to syncline stacks

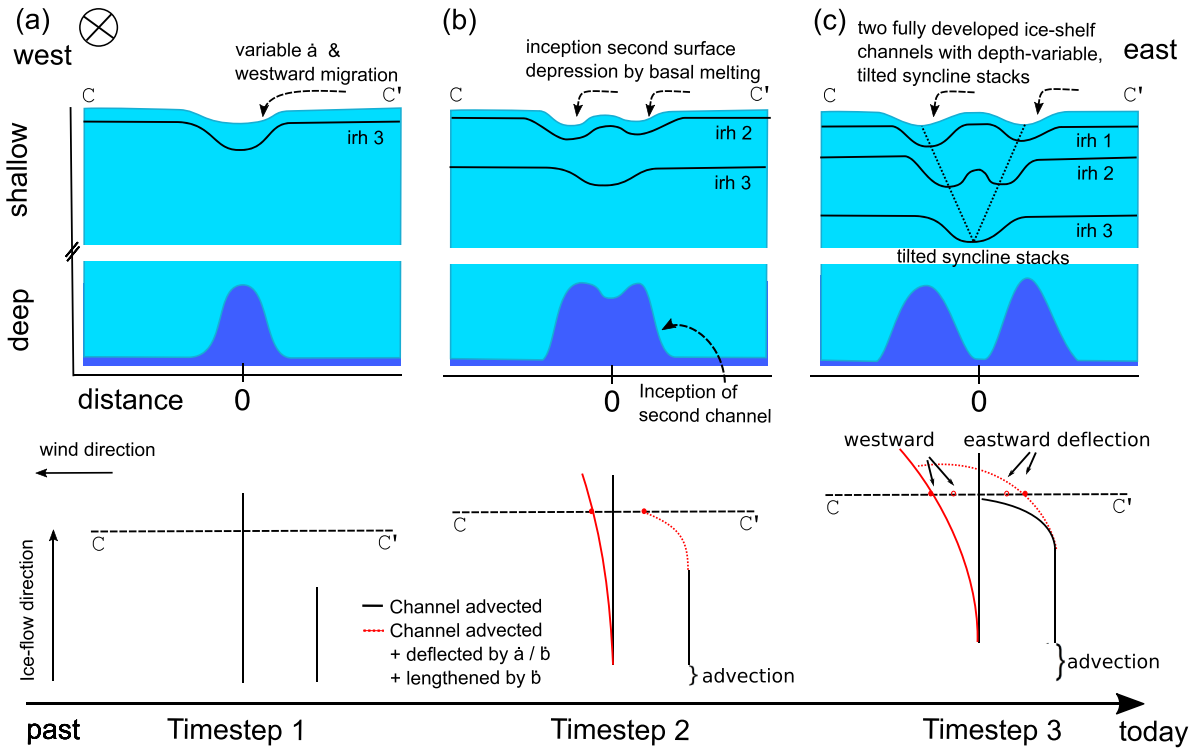

Figure 12. Scenario for the radar Cross Section C-C′ (top) witnessing a breakthrough of an ice shelf channel junction that was initially located farther upstream. The corresponding bird's eye perspective of the ice shelf channel geometry is shown at the bottom, with the temporal evolution displayed from left to right. In (a) existence of a single ice shelf channel is reflected in the internal radar stratigraphy (irhs 1–3) with a syncline caused by variability in $\dot{a}$. Breakthrough of the ice shelf channel junction (b) causes formation of two syncline stacks. Progressive deflection of both channels into opposite direction cause further tilting of syncline stacks in opposing directions. Existence of a single ice shelf channel is still visible in irh 3 (c).

with opposite tilt direction. It cannot uniquely be determined what caused the formation and then deflection of the second ice shelf channel at Time Step 2. The variability of $\dot{a}$ forming the syncline stacks only starts after the surface depression has already evolved. A possible mechanism for the evolution of the surface depression is localized basal melting eventually linking both ice shelf channels at Junction J3. Truncated radar stratigraphy at the basal flanks of the eastern ice shelf channels is a possible relict of such locally elevated basal melting (e.g., Profile D-D′; supporting information). Satellite imagery of an ice shelf channel in the Getz ice shows that basal melting can be highly localized at ice shelf channel heads far from the grounding line (Alley et al., 2016). At the Roi Baudouin Ice Shelf, time series analysis of satellite imagery does not show significant modification of the ice shelf channel junction prior to 1996. This highlights the usefulness of the internal radar stratigraphy as proxy for ice-atmosphere and ice-ocean interactions which could very well go back to hundreds of years if fully explored.

5.4. Interpretation of the Ice Shelf Channel Morphology

Our initial goals were to evaluate the two hypotheses: (1) if ice shelf channel deflections are caused by processes occurring at the grounding line (e.g., migration of subglacial water outlets) or if deflections are caused by atmospheric and oceanic processes occurring farther seaward. And (2) if ice shelf channel junctions are formed by splitting/merging of ice shelf channel sources at the grounding line or by other oceanic processes occurring farther seaward. We identified two novel mechanisms changing the ice shelf morphology during advection seaward of the grounding line. First, some ice shelf channels are deflected on longer wavelengths due to a spatially variable $\dot{a}$. Second, an ice shelf channel junction likely formed at the center of the ice shelf. Those processes act in addition to other known mechanisms during ice shelf advection such as asymmetric ocean-driven melting (Gladish et al., 2012; Gourmelen et al., 2017; Sergienko, 2013) and ice shelf channels growing landward (Alley et al., 2016). The radar data near the grounding line (Figure 4) show truncated layers at the ice shelf base testifying to localized basal melting as established previously for other ice shelf

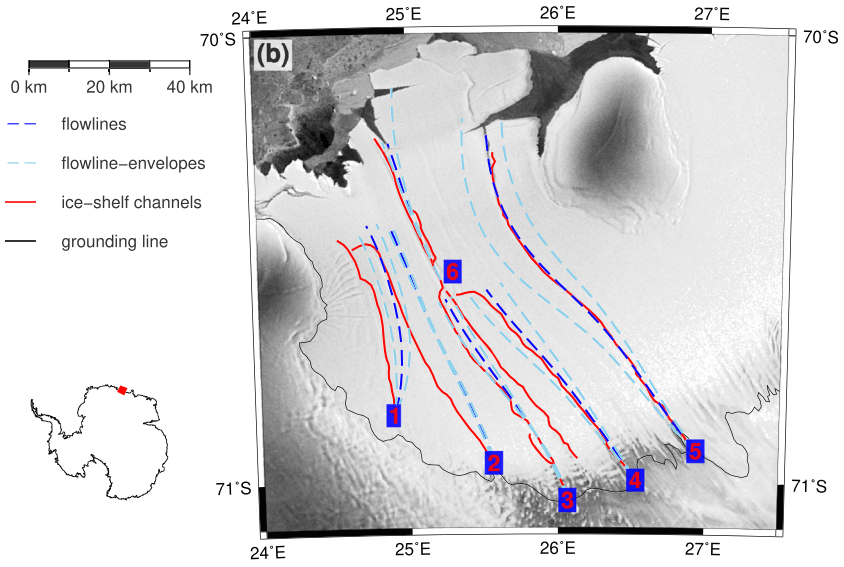

Figure 13. Ice shelf channels and corresponding flowlines with seed points numbered 1–6. The flowline envelopes are traced for a velocity field assuming a constant ±10% bias in the flow vector components.

channels (Marsh et al., 2016). This basal melting, in conjunction with variable subglacial water outlet positions, may be strong enough to create the sharp angled junctions east of Ice Shelf Channel 4 (Figure 1a) in a comparatively short time interval (Le Brocq et al., 2013). This means that both Hypothesis 1 and Hypothesis 2 (Figure 3) are inadequate to explain the ice shelf morphology alone. All processes at and seaward of the grounding line must be included. Analysis of the internal radar stratigraphy may be one way forward to achieve this.

The observed tilts in the syncline stacks of the shallow radar stratigraphy reflect a leftward deflection of Ice Shelf Channels 4 and 6. We have inferred that this deflection is caused at least in parts by a spatially variable $\dot{a}$. The deflection may well be reinforced by variable $\dot{b}$. The deeper layers truncate within the ice shelf channels at the base, but whether or not this feature is inherited from basal melting near the grounding zone is unclear. Although details about how Ice Shelf Channel Junction J3 as formed are not particularly well constrained, the timing and hence location where this event has taken place are far away from the grounding line. Localized basal melting is one possibility for connecting the ice shelf channels in the center of the shelf. Other mechanisms may also be important, for example, the converging Junction J4 (Figure 2) is located in an area where across-flow basal crevassing is evident in the surface elevation model. It is possible that such basal crevasses connect two neighboring ice shelf channels, and act as seed points for localized basal melting further incising the ice shelf from below.

Interpretation of the ice shelf channel morphology relative to today's flow field presupposes both that ice flow direction is correctly observed today and that it has not changed significantly in the past. The first assumption is not trivial, as residual phase ramps using satellite based interferometric synthetic aperture radar data may occur unnoticed (e.g., from incorrectly estimating orbital parameters Drews et al., 2009). The flowline accumulates these biases eventually leading to an apparent deflection. We quantified this uncertainty by introducing an artificial bias in the flow vector components of ±10%. The resulting flowline envelopes then still show a significant leftward deflection for Ice Shelf Channels 1, 2, and 6 (Figure 13). Temporal changes of the flow vector, on the other hand, are unlikely to result in a tilted syncline stack assuming that mechanisms for the syncline formation are tied to the changes in ice thickness. Changes in ice flow direction would likely occur over the entire ice column without shearing. The observed tilt is therefore a signature of gradual modification of ice shelf channel morphology by atmospheric and possibly also oceanic processes.

In summary, analysis of the isochronal radar stratigraphy is important for interpretation of ice shelf channel morphology as it is the only method encompassing ice dynamic, oceanographic, and atmospheric history over decadal to centennial timescales. Additional theoretical work is needed to identify necessary and sufficient conditions for formation of junctions as well as for variability in $\dot{a}$ and $\dot{b}$ across ice shelf channels.

From the observational side, more contemporary evidence of changing ice shelf channel morphology from satellite data is needed.

6. Conclusion

We have analyzed radar data across ice shelf channels in the Roi Baudouin Ice Shelf and modeled the radar stratigraphy for 2-D transects. The combination of both techniques enables interpretation of the radar stratigraphy as proxy for atmospheric and oceanic processes. There are several findings. First, ice shelf stratigraphy is 9 times more sensitive to spatial variability in the net surface accumulation/ablation rate than to spatial variability in the net basal melting/freezing rate. Second, shallow syncline/anticline stacks in ice shelf channels can be interpreted by increased snow deposition at the upwind side and wind erosion at the downwind side. Third, this spatial variability causes a westward deflection of the ice shelf channels. The deflection is recorded in the radar stratigraphy by tilting syncline stacks. The tilt together with a depth-age estimate can be used to infer deflection rates which, for Roi Baudouin Ice Shelf, are several meters per year. Fourth, elevated basal melting is evidenced by truncating radar layers at the ice shelf base both near the grounding line and farther seaward. The contribution of basal melting to syncline formation in ice shelf channels is partially masked by the dominant signal from the net surface accumulation/ablation rate. Fifth, we interpret depth variable syncline structures at an ice shelf channel junction to be caused by localized basal melting forming an ice shelf channel junctions during ice advection in the center of the ice shelf.

The ice shelf channel morphology is therefore a rich proxy for atmospheric and oceanographic processes acting on various temporal and spatial scales. However, it is not simple to attribute these observations to a single mechanism, and our observations require that atmospheric and oceanographic processes seaward of the grounding line are included.

Appendix A: Estimating the Age-Depth Relationship in the Firn Column

Plugging equation (3) into equation (2) for the vertical velocity results in

$$\left(\rho_i - (\rho_i - \rho_s)e^{-kz}\right)\frac{\partial u_z}{\partial z} + (\rho_i - \rho_s)ke^{-kz}u_z = 0 \tag{A1}$$

This differential equation is separable and result in

$$u_z = c_1\frac{e^{kz}}{\rho_i(e^{kz}-1)+\rho_s} \tag{A2}$$

The integration constant $c_1 = \dot{a}_s$ (where $\dot{a}_s$ is the net surface accumulation/ablation rate in units kg^2 m^{-2} a^{-1}) sets the surface velocity $u_z(z=0) = \frac{\dot{a}_s}{\rho_s}$ (Eisen, 2008). This holds for zero basal melting and no along-flow stretching. While the cumulative effect of along-flow stretching in the young and shallow firn is small, omission of basal melting is not justified everywhere. We account for this by considering a wide range for $\dot{a}_s$ (200–800 kg m^{-2} a^{-1}) corresponding to the maximum and minimum values observed at Roi Baudouin Ice Shelf (Lenaerts et al., 2014). This correspondingly results in a wide range of vertical velocity profiles bracketing many areas with basal melting. Using this form of the vertical velocity results in an analytical solution for the steady-state age equation,

$$c_1\frac{e^{kz}}{\rho_i(e^{kz}-1)+\rho_s}\frac{\partial A(z)}{\partial z} = 1 \tag{A3}$$

which is

$$A(z) = \frac{\rho_i - \rho_s}{c_1 k}e^{-kz} + \frac{\rho_i}{c_1}z + c_2 \tag{A4}$$

The second integration constant is determined using $A(z=0)=0$, so that $c_2 = -\frac{\rho_i-\rho_s}{c_1 k}$.

Appendix B: Vertical Velocities for a Flowline of a Freely Floating Ice Shelf

We assume that the vertical velocity $u_z(z)$ in a hydrostatically balanced ice shelf can be described with two terms:

$$u_z = u_{\text{col. adj.}} + u_{\text{thin.}} \tag{B1}$$

where $u_{\text{col. adj.}}$ describes the column adjustment as a function of $\dot{a}$ and $\dot{b}$ and $u_{\text{thin.}}$ describes dynamic thinning in the along-flow direction. We calculate the dynamic thinning term using the incompressibility condition:

$$\frac{\partial u_x}{\partial x} + \frac{\partial u_{\text{thin}}}{\partial z} = 0 \tag{B2}$$

with the along-flow velocities u_x. After integration from the surface ($z = 0$) down to depth z this results in

$$u_{\text{thin.}}(z) = u_{z=0,\text{thin}} + z\frac{\partial u_x}{\partial x} \tag{B3}$$

assuming that the horizontal strain rate $\frac{\partial u_x}{\partial x}$ does not have a depth dependence. This is valid in large parts of ice shelves (Morland, 1987), making the vertical velocity profile a linear function of depth. We determine the integration constant $u_{z=0,thin}$ by imposing flotation on ice thickness changes $\dot{H}$:

$$\dot{H} = u_{z=0,\text{thin}} - u_{z=B,\text{thin}} = z_B\frac{\partial u_x}{\partial x}. \tag{B4}$$

The index B marks the ice shelf base (so that $z_B = \text{H}$ as $z = 0$ was defined at the surface), and flotation requires

$$u_{z=0,\text{thin.}} = \dot{H}(1 - \frac{\rho_i}{\rho_w}) = H(1 - \frac{\rho_i}{\rho_w})\frac{\partial u_x}{\partial x} \tag{B5}$$

The vertical velocities induced by $\dot{a}$ and $\dot{b}$ are independent of depth:

$$u_{z,\text{col. adj.}} = \dot{a}\frac{\rho_i}{\rho_w} + \dot{b}\left(1 - \frac{\rho_i}{\rho_w}\right) \tag{B6}$$

This equation can be understood as column adjustment to regain hydrostatic equilibrium after any mass changes. The adjustment is more sensitive to mass changes at the surface than to changes at the base (e.g., ice added to the surface causes lowering of the ice column modulated with a factor ~ 0.9; ice removal from the base causes lowering of the ice column modulated with a factor $\sim$0.1). Adding the column adjustment and dynamic thinning results in

$$u_z(z) = \dot{a}\frac{\rho_i}{\rho_w} + \dot{b}(1 - \frac{\rho_i}{\rho_w}) + \left(H(1 - \frac{\rho_i}{\rho_w}) + z\right)\frac{\partial u_x}{\partial x} \tag{B7}$$

Acknowledgments
We thank the reviewers, the Associate Editor, and the Editor for extensive, detailed, and constructive feedback that has significantly improved the paper. Fieldwork in 2012 and 2014 was funded by the InBev Baillet Latour Antarctica Fellowship and the ICECON project of the Belgian Science Policy Office (BELSPO; Project SD/CA/96A). R. Drews was supported by an Emmy Noether Grant of the Deutsche Forschungsgemeinschaft (DR 822/3-1). Rupert Gladstone's contribution was supported by Academy of Finland Grants 286587 and 322430. C. Schannwell was supported by the Deutsche Forschungsgemeinschaft in the framework of the priority programme "Antarctic Research with comparative investigations in Arctic ice areas" by the Grant EH 329/13-1. We thank J. T. Lenaerts and B. Van Liefferinge for collecting the 400 MHz data in 2014. We acknowledge the efficient logistical support from the International Polar Foundation, Antarctic, and the Belgian Military during all fieldwork. We also thank the Elmer/Ice developers for making their code available, C. Martín for helping out with details in the Age Solver, and P. Bons for constructive discussions. We gratefully acknowledge the Generic Mapping Tool as well as the compute and data resources provided by the Leibniz Supercomputing Centre (www.lrz.de). The authors declare no conflict of interest. Radar data are available at the Pangaea Data Archive (https://doi.pangaea.de/10.1594/PANGAEA.907146). Surface elevation, hydrostatic ice thickness, and net basal melt/freezing rates of the Roi Baudouin Ice Shelf are available online (https://doi.org/10.1594/PANGAEA.883285).

References

Alley, K. E., Scambos, T. A., Siegfried, M. R., & Fricker, H. A. (2016). Impacts of warm water on Antarctic ice shelf stability through basal channel formation. *Nature Geoscience*, *9*, 290–293.

Asay-Davis, X. S., Cornford, S. L., Durand, G., Galton-Fenzi, B. K., Gladstone, R. M., Gudmundsson, G. H., et al. (2016). Experimental design for three interrelated marine ice sheet and ocean model intercomparison projects: MISMIP v. 3 (MISMIP +), ISOMIP v. 2 (ISOMIP +) and MISOMIP v. 1 (MISOMIP1). *Geoscientific Model Development*, *9*(7), 2471–2497.

Bell, R. E., Chu, W., Kingslake, J., Das, I., Tedesco, M., Tinto, K. J., et al. (2017). Antarctic ice shelf potentially stabilized by export of meltwater in surface river. *Nature*, *544*(7650), 344–348.

Berger, S., Drews, R., Helm, V., Sun, S., & Pattyn, F. (2017). Detecting high spatial variability of ice shelf basal mass balance, Roi Baudouin Ice Shelf, Antarctica. *The Cryosphere*, *11*(6), 2675–2690.

Berger, S., Favier, L., Drews, R., Derwael, J.-J., & Pattyn, F. (2016). The control of an uncharted pinning point on the flow of an Antarctic ice shelf. *Journal of Glaciology*, *62*(231), 37–45.

Black, H., & Budd, W. (1964). Accumulation in the region of Wilkes, Wilkes Land. *Antarctica*, *5*(37), 3–15.

Bons, P. D., Kleiner, T., Llorens, M.-G., Prior, D. J., Sachau, T., Weikusat, I., & Jansen, D. (2018). Greenland ice sheet: Higher nonlinearity of ice flow significantly reduces estimated basal motion. *Geophysical Research Letters*, *45*, 6542–6548. https://doi.org/10.1029/2018GL078356

Callens, D., Drews, R., Witrant, E., Philippe, M., & Pattyn, F. (2016). Temporally stable surface mass balance asymmetry across an ice rise derived from radar internal reflection horizons through inverse modeling. *Journal of Glaciology*, *62*(233), 1–10.

Dow, C. F., Lee, W. S., Greenbaum, J. S., Greene, C. A., Blankenship, D. D., Poinar, K., et al. (2018). Basal channels drive active surface hydrology and transverse ice shelf fracture. *Science Advances*, *4*(6), eaao7212.
Drews, R. (2015). Evolution of ice-shelf channels in Antarctic ice shelves. *The Cryosphere*, *9*, 1169–1181.
Drews, R., Brown, J., Matsuoka, K., Witrant, E., Philippe, M., Hubbard, B., & Pattyn, F. (2016). Constraining variable density of ice shelves using wide-angle radar measurements. *The Cryosphere*, *10*(2), 811–823.
Drews, R., Eisen, O., Weikusat, I., Kipfstuhl, S., Lambrecht, A., Steinhage, D., et al. (2009). Layer disturbances and the radio-echo free zone in ice sheets. *The Cryosphere*, *3*, 195–203.
Drews, R., Martn, C., Steinhage, D., & Eisen, O. (2013). Characterizing the glaciological conditions at Halvfarryggen ice dome, Dronning Maud Land, Antarctica. *Journal of Glaciology*, *59*(213), 9–20.
Drews, R., Matsuoka, K., Martn, C., Callens, D., Bergeot, N., & Pattyn, F. (2015). Evolution of Derwael Ice Rise in Dronning Maud Land, Antarctica, over the last millennia. *Journal of Geophysical Research: Earth Surface*, *120*, 564–579. https://doi.org/10.1002/2014JF003246
Drews, R., Pattyn, F., Hewitt, I. J., Ng, F. S. L., Berger, S., Matsuoka, K., et al. (2017). Actively evolving subglacial conduits and eskers initiate ice shelf channels at an Antarctic grounding line. *Nature Communications*, *8*, 15,228.
Dupont, T. K., & Alley, R. B. (2005). Assessment of the importance of ice-shelf buttressing to ice-sheet flow. *Geophysical Research Letters*, *32*, L04503. https://doi.org/10.1029/2004GL022024
Durand, G., Gagliardini, O., de Fleurian, B., Zwinger, T., & Le Meur, E. (2009). Marine ice sheet dynamics: Hysteresis and neutral equilibrium. *Journal of Geophysical Research*, *114*, F03009. https://doi.org/10.1029/2008JF001170
Dutrieux, P., Stewart, C., Jenkins, A., Nicholls, K. W., Corr, H. F. J., Rignot, E., & Steffen, K. (2014). Basal terraces on melting ice shelves. *Geophysical Research Letters*, *41*, 5506–5513. https://doi.org/10.1002/2014GL060618
Dutrieux, P., Vaughan, D. G., Corr, H. F. J., Jenkins, A., Holland, P. R., Joughin, I., & Fleming, A. H. (2013). Pine Island glacier ice shelf melt distributed at kilometre scales. *The Cryosphere*, *7*(5), 1543–1555.
Eisen, O. (2008). Inference of velocity pattern from isochronous layers in firn, using an inverse method. *Journal of Glaciology*, *54*(187), 613–630.
Eisen, O., Nixdorf, U., Wilhelms, F., & Miller, H. (2004). Age estimates of isochronous reflection horizons by combining ice core, survey, and synthetic radar data. *Journal of Geophysical Research*, *109*, B04106. https://doi.org/10.1029/2003JB002858
Fürst, J. J., Durand, G., Gillet-chaulet, F., Tavard, L., Rankl, M., Braun, M., & Gagliardini, O. (2016). The safety band of Antarctic ice shelves. *Nature Climate Change*, *6*, 479–482.
Fujita, S., Maeno, H., & Matsuoka, K. (2006). Radio-wave depolarization and scattering within ice sheets: A matrix-based model to link radar and ice-core measurements and its application. *Journal of Glaciology*, *52*(178), 407–424.
Gagliardini, O., Zwinger, T., Gillet-Chaulet, F., Durand, G., Favier, L., de Fleurian, B., et al. (2013). Capabilities and performance of Elmer/Ice, a new-generation ice sheet model. *Geoscientific Model Development*, *6*(4), 1299–1318.
Gladish, C. V., Holland, D. M., Holland, P. R., & Price, S. F. (2012). Ice-shelf basal channels in a coupled ice/ocean model. *Journal of Glaciology*, *58*(212), 1227–1244.
Goldberg, D. N., Gourmelen, N., Kimura, S., Millan, R., & Snow, K. (2019). How accurately should we model ice shelf melt rates? *Geophysical Research Letters*, *46*, 189–199. https://doi.org/10.1029/2018GL080383
Goldsby, D. L., & Kohlstedt, D. L. (2001). Superplastic deformation of ice: Experimental observations. *Journal of Geophysical Research*, *106*(B6), 11,017–11,030.
Gourmelen, N., Goldberg, D. N., Snow, K., Henley, S. F., Bingham, R. G., Kimura, S., et al. (2017). Channelized melting drives thinning under a rapidly melting Antarctic ice shelf: Ice shelves channel melting and thinning. *Geophysical Research Letters*, *44*, 9796–9804. https://doi.org/10.1002/2017GL074929
Greene, C. A., Gwyther, D. E., & Blankenship, D. D. (2017). Antarctic mapping tools for Matlab. *Computers & Geosciences*, *104*, 151–157.
Hubbard, B., Tison, J. L., Philippe, M., Heene, B., Pattyn, F., Malone, T., & Freitag, J. (2013). Ice shelf density reconstructed from optical televiewer borehole logging. *Geophysical Research Letters*, *40*, 5882–5887. https://doi.org/10.1002/2013GL058023
Jenkins, A. (2011). Convection-driven melting near the grounding lines of ice shelves and tidewater glaciers. *Journal of Physical Oceanography*, *41*(12), 2279–2294.
Jeofry, H., Ross, N., Le Brocq, A., Graham, A. G. C., Li, J., Gogineni, P., et al. (2018). Hard rock landforms generate 130 km ice shelf channels through water focusing in basal corrugations. *Nature Communications*, *9*(1), 4576. https://doi.org/10.1038/s41467-018-06679-z
Jezek, K. C. (2003). Observing the Antarctic ice sheet using the RADARSAT-1 synthetic aperture radar. *Polar Geography*, *27*(3), 197–209.
Jezek, K. C., Alley, R. B., & Thomas, R. H. (1985). Rheology of glacier ice. *Science*, *227*(4692), 1335–1337.
Langley, K., von Deschwanden, A., Kohler, J., Sinisalo, A., Matsuoka, K., Hattermann, T., et al. (2014). Complex network of channels beneath an Antarctic ice shelf: Langley et. al.; Channels beneath Antarctic ice shelf. *Geophysical Research Letters*, *41*, 1209–1215. https://doi.org/10.1002/2013GL058974
Le Brocq, A. M., Ross, N., Griggs, J. A., Bingham, R. G., Corr, H. F. J., Ferraccioli, F., et al. (2013). Evidence from ice shelves for channelized meltwater flow beneath the Antarctic Ice Sheet. *Nature Geoscience*, *6*(10), 1–4.
Lenaerts, J. T. M., Brown, J., Van Den Broeke, M. R., Matsuoka, K., Drews, R., Callens, D., et al. (2014). High variability of climate and surface mass balance induced by Antarctic ice rises. *Journal of Glaciology*, *60*(224), 1101–1110.
Lenaerts, J. T. M., Lhermitte, S., Drews, R., Ligtenberg, S. R. M., Berger, S., Helm, V., et al. (2017). Meltwater produced by wind-albedo interaction stored in an East Antarctic ice shelf. *Nature Climate Change*, *7*(1), 58–62.
Lenaerts, J. T. M., Medley, B., Broeke, M. R., & Wouters, B. (2019). Observing and modeling ice sheet surface mass balance. *Reviews of Geophysics*, *57*, 376–420. https://doi.org/10.1029/2018RG000622
Mankoff, K. D., Jacobs, S. S., Tulaczyk, S. M., & Stammerjohn, S. E. (2012). The role of Pine Island Glacier ice shelf basal channels in deep-water upwelling, polynyas and ocean circulation in Pine Island Bay, Antarctica. *Annals of Glaciology*, *53*(60), 123–128.
Marsh, O. J., Fricker, H. A., Siegfried, M. R., Christianson, K., Nicholls, K. W., Corr, H. F. J., & Catania, G. (2016). High basal melting forming a channel at the grounding line of Ross Ice Shelf, Antarctica. *Geophysical Research Letters*, *43*, 250–255. https://doi.org/10.1002/2015GL066612
Martin, M. A., Winkelmann, R., Haseloff, M., Albrecht, T., Bueler, E., Khroulev, C., & Levermann, A. (2011). The Potsdam Parallel Ice Sheet Model (PISM-PIK) âĂŞ Part 2: Dynamic equilibrium simulation of the Antarctic ice sheet. *The Cryosphere*, *5*(3), 727–740.
Millgate, T., Holland, P. R., Jenkins, A., & Johnson, H. L. (2013). The effect of basal channels on oceanic ice-shelf melting. *Journal of Geophysical Research: Oceans*, *118*, 6951–6964. https://doi.org/10.1002/2013JC009402
Morland, L. W. (1987). Unconfined ice-shelf flow. In C. J. van der Veen & J. Oerlemans (Eds.), *Dynamics of the West Antarctic Ice Sheet* (pp. 99–116). Netherlands: Kluwer Acad., Dordrecht.
Mouginot, J., Scheuchl, B., & Rignot, E. (2012). Mapping of ice motion in Antarctica using synthetic-aperture radar data. *Remote Sensing*, *4*(9), 2753–2767.

Pattyn, F., Matsuoka, K., Callens, D., Conway, H., Depoorter, M., Docquier, D., et al. (2012). Melting and refreezing beneath Roi Baudouin Ice Shelf (East Antarctica) inferred from radar, GPS, and ice core data. *Journal of Geophysical Research*, *117*, F04008. https://doi.org/10.1029/2011JF002154

Philippe, M., Tison, J.-L., Fjøsne, K., Hubbard, B., Kjr, H. A., Lenaerts, J. T. M., et al. (2016). Ice core evidence for a 20th century increase in surface mass balance in coastal Dronning Maud Land, East Antarctica. *The Cryosphere*, *10*(5), 2501–2516.

Rack, W., & Rott, H. (2004). Pattern of retreat and disintegration of the Larsen B ice shelf, Antarctic Peninsula. *Annals of Glaciology*, *39*, 505–510.

Rignot, E., & Steffen, K. (2008). Channelized bottom melting and stability of floating ice shelves. *Geophysical Research Letters*, *35*, L02503. https://doi.org/10.1029/2007GL031765

Schannwell, C., Cornford, S., Pollard, D., & Barrand, N. E. (2018). Dynamic response of Antarctic Peninsula Ice Sheet to potential collapse of Larsen C and George VI ice shelves. *The Cryosphere*, *12*(7), 2307–2326.

Sergienko, O. V. (2013). Basal channels on ice shelves. *Journal of Geophysical Research: Earth Surface*, *118*, 1342–1355. https://doi.org/10.1002/jgrf.20105

Shean, D. E., Joughin, I. R., Dutrieux, P., Smith, B. E., & Berthier, E. (2018). Ice shelf basal melt rates from a high-resolution DEM record for Pine Island Glacier, Antarctica. *The Cryosphere Discussions*, *13*(10), 2633–2656. https://doi.org/10.5194/tc-13-2633-2019

Spikes, V. B., Hamilton, G. S., Arcone, S. A., Kaspari, S., & Mayewski, P. A. (2004). Variability in accumulation rates from GPR profiling on the West Antarctic plateau. *Annals of Glaciology*, *39*, 238–244.

Stanton, T. P., Shaw, W. J., Truffer, M., Corr, H. F. J., Peters, L. E., Riverman, K. L., et al. (2013). Channelized ice melting in the ocean boundary layer beneath Pine Island Glacier, Antarctica. *Science*, *341*(6151), 1236–1239.

Sun, S., Hattermann, T., Pattyn, F., Nicholls, K. W., Drews, R., & Berger, S. (2019). Topographic shelf waves control seasonal melting near Antarctic ice shelf grounding lines. *Geophysical Research Letters*, *46*(16). https://doi.org/10.1029/2019GL083881

Vaughan, D. G., Corr, H. F. J., Bindschadler, R. A., Dutrieux, P., Gudmundsson, G. H., Jenkins, A., et al. (2012). Subglacial melt channels and fracture in the floating part of Pine Island Glacier, Antarctica. *Journal of Geophysical Research*, *117*, F03012. https://doi.org/10.1029/2012JF002360

Washam, P., Nicholls, K. W., Münchow, A., & Padman, L. (2019). Summer surface melt thins Petermann Gletscher Ice Shelf by enhancing channelized basal melt. *Journal of Glaciology*, *65*(252), 662–674.

Wearing, M., Stevens, L. A., Dutrieux, P., & Kingslake, J. (2018). Ice-shelf secondary flow counteracts growth of sub-ice-shelf channels. AGU Fall Meeting Abstracts.